Final Scientific/Technical Report

DE-SC0002594

First-Principles Petascale Simulations for Predicting Deflagration to Detonation Transition in Hydrogen-Oxygen Mixtures

A. Khokhlov[1](PI), J. Austin[2](Co-I), C. Bacon[3](Co-I)

March 2, 2015

[1]Dept. of Astronomy and Astrophysics and the Enrico Fermi Institute, The University of Chicago, Chicago, IL

[3]Argonne Leadership Computing Facility, Argonne National Laboratory, Chicago, IL

[2]Department of Aerospace Engineering, The University of Illinois at Urbana-Champaign, IL

1 Executive summary

Hydrogen has emerged as an important fuel across a range of industries as a means of achieving energy independence and to reduce emissions. DDT and the resulting detonation waves in hydrogen-oxygen can have especially catastrophic consequences in a variety of industrial and energy producing settings related to hydrogen. First-principles numerical simulations of flame acceleration and DDT are required for an in-depth understanding of the phenomena and facilitating design of safe hydrogen systems.

The goals of this project were (1) to develop first-principles petascale reactive flow Navier-Stokes simulation code for predicting gaseous high-speed combustion and detonation (HSCD) phenomena and (2) demonstrate feasibility of first-principles simulations of rapid flame acceleration and deflagration-to-detonation transition (DDT) in stoichiometric hydrogen-oxygen mixture ($2H_2 + O_2$).

The goals of the project have been accomplished. We have developed a novel numerical simulation code, named HSCD, for performing first-principles direct numerical simulations of high-speed hydrogen combustion. We carried out a series of validating numerical simulations of inert and reactive shock reflection experiments in shock tubes. We then performed a pilot numerical simulation of flame acceleration in a long pipe. The simulation showed the transition of the rapidly accelerating flame into a detonation. The DDT simulations were performed using BG/Q Mira at the Argonne National Laboratiory, currently the fourth fastest super-computer in the world.

The HSCD is currently being actively used on BG/Q Mira for a systematic study of the DDT processes using computational resources provided through the 2014-2016 INCITE allocation "First-principles simulations of high-speed combustion and detonation."

While the project was focused on hydrogen-oxygen and on DDT, with appropriate modifications of the input physics (reaction kinetics, transport coefficients, equation of state) the code has a much broader applicability to petascale simulations of high speed combustion and detonation phenomena in reacting gases, and to high speed viscous gaseous flows in general.

Project activities included three major steps – (1) development of physical and numerical models, (2) code validation, and (3) demonstration simulation of flame acceleration and DDT in a long pipe. These steps are documented in the following sections below.

2 Physical model

HSCD regime in general is a regime in which fluid velocities encompass the range from subsonic to supersonic; Mach numbers may be $M > 1$. In these conditions both the compressibility of matter and shock waves are important. The HSCD code developed in this project was specifically designed to deal with shocks and compressible turbulence, in addition to effects of chemistry, viscous, heat, and mass diffusion, radiation losses, sound waves, turbulence and boundary layers which are are present in low Mach number combustion regimes as well. Many existing codes can treat the low-speed combustion regimes but have difficulty dealing with shocks, compressibility, shock-flame, and shock-turbulence interactions. The HSCD code can deal with both the low Mach number flame propagation and with rapidly moving turbulent flames, detonation waves, and transient DDT phenomena. The physical model incorporated into HSCD described

2.1 Governing equations

The governing equations describing the HSCD regime consist of compressible, reactive flow Navier-Stokes (NS) equations of fluid dynamics augmented with appropriate sub-models for chemical kinetics and microscopic transport. The NS equations in conservative form are [1],

$$\frac{\partial \rho}{\partial t} = -\nabla \cdot (\rho \mathbf{u}) \,, \tag{1}$$

$$\frac{\partial \rho \mathbf{u}}{\partial t} = -\nabla \cdot \left(\rho \mathbf{u} \otimes \mathbf{u} + P \, \hat{\mathbf{I}} + \hat{\pi} \right) , \tag{2}$$

$$\frac{\partial E}{\partial t} = -\nabla \cdot \left(\mathbf{u} \left(E + P \right) + \mathbf{u} \cdot \hat{\pi} + \mathbf{q}^e \right) , \tag{3}$$

$$\frac{\partial \rho \mathcal{Y}_i}{\partial t} = -\nabla \cdot \left(\rho \mathbf{u} \mathcal{Y}_i + \mathbf{q}^i \right) + \rho \mathcal{R}_i, \quad i = 1, ..., N, \tag{4}$$

where ρ is the mass density, $\mathbf{u}$ is the fluid velocity, P is the pressure, $E = \rho e + \frac{1}{2}\rho u^2$ is the total energy density, e is the internal energy per unit mass, $\mathcal{Y}_i$ are chemical variables, N is the total number of reactants, $\hat{\mathbf{I}}$ is a unit tensor, $\hat{\pi}$ is the viscous stress tensor, $\mathbf{q}^e$ is the heat diffusion flux, $\mathbf{q}^i$ are diffusion fluxes of reactants, and $\mathcal{R}_i$ are the chemical reaction terms (Sect. 2.2).

Chemical variables $\mathcal{Y}_i$ have the meaning of *moles of reactants per unit mass*,

$$\mathcal{Y}_i = n_i/\rho N_a, \quad i = 1, ..., N, \tag{5}$$

where n_i are the number densities of reactants and N_a is the Avogadro number. Due to the mass conservation

$$\sum_{i=1}^{N} m_i \mathcal{Y}_i = 1, \tag{6}$$

where m_i are molecular weights of reactants. Note that with $\mathcal{Y}_i$ defined by (5), the mass fluxes due to diffusion of individual reactants are equal to $m_i \mathbf{q}^i$. For a reference we mention the relations of $\mathcal{Y}_i$ to other chemical variables frequently used in the literature are as follows: partial mass densities, $\rho_i = \rho m_i \mathcal{Y}_i$; mass fractions, $Y_i = m_i \mathcal{Y}_i$; molar fractions, $X_i = \mathcal{M}\mathcal{Y}_i$; molar concentrations $[\mathcal{S}_i] = \rho \mathcal{Y}_i$, where $\mathcal{S}_i$ are chemical symbols of reactants. Using $\mathcal{Y}_i$ is convenient because $\mathcal{Y}_i$ enter into the kinetic equations in the same simple way as $[\mathcal{S}_i]$. At the same time, $\mathcal{Y}_i$ do not vary with density or pressure when the chemical composition of the mixture is fixed. Table 1 gives a full list of variables used in this report.

2.2 Reaction mechanism

The HSCD code utilises a reaction mechanism of O'Conair etal. [2] which incorporates $N = 8$ reaction species, H, H_2, O, O_2, OH, H_2O, HO_2, and H_2O_2; see Table 2 for a list of reactions and reaction constants. For a reactant, k, participating in a reaction represented by $\sum_{i=1}^{N} \nu_{i,k}^f \mathcal{S}_i \rightleftharpoons \sum_{i=1}^{N} \nu_{i,k}^b \mathcal{S}_i$, where subscripts f and b stand for forward and backward, the reaction terms $\mathcal{R}_k$ is given by

$$\mathcal{R}_k = k^f \rho^{n_f - 1} \prod_{i=1}^{N} \mathcal{Y}_i^{\nu_{i,k}^f} - k^b \rho^{n_b - 1} \prod_{i=1}^{N} \mathcal{Y}_i^{\nu_{i,k}^b}, \tag{7}$$

Table 1: Nomenclature

Symbol	Definition	Units
ρ	Mass density	g/cm^3
P	Pressure	erg/cm^3
E	Energy density	erg/cm^3
π	Viscous stress tensor	erg/cm^3
e	Internal energy per unit mass	erg/g
h	Enthalpy per unit mass	erg/g
$\mathbf{u}$	Bulk fluid velocity	cm/s
$\mathbf{q}^e$	Energy flux due to microscopic transport	ergs/cm^2/s
a_s	Sound speed	cm/s
μ	Physical viscosity	g/cm/s
ν	Kinematic viscosity	cm^2/s
λ	Thermal conductivity	erg/cm^2/s/K
C_p	Specific heat at constant pressure	erg/g/K
R_g	Gas constant	erg/g/K
N_a	Avogadro number	
$\mathcal{M}$	Mean molecular weight	
m_i	Molecular weights of individual reactants	
D_{ik}	Binary diffusion coefficients	cm^2/s
$\mathbf{u}^i$	Diffusion velocities	cm/s
$\mathbf{q}^i$	Diffusion fluxes	g/cm^2/s
$C^0_{p,i}$	Specific heats of individual reactants	ergs/mole/K
$H^0_{p,i}$	Enthalpies of individual reactants	ergs/mole

where $n_f = \sum_{i=1}^{N} \nu_{i,k}^f$, $n_b = \sum_{i=1}^{N} \nu_{i,k}^b$, and k_f and k_b are forward and backward reaction rates. Forward reaction rates for all reactions are calculated according to

$$k_f = AT^{\beta} e^{-Q/R_g T} \tag{8}$$

with coefficients A, β, and Q provided in Table 2 except of reactions No.9 and No.15 which are calculated using Troe's pressure falloff approximation [3],

$$k_f = k_\infty \frac{P_r}{1+P_r} F, \tag{9}$$

$$P_r = \frac{k_o}{k_\infty} [M], \quad [M] = \rho \sum_{i=1}^{N} f_i \mathcal{Y}_i, \tag{10}$$

$$F = F_c \exp\left(\left(1 + \left(\frac{\log P_r + c}{n - d(\log P_r + c)} \right)^2 \right)^{-1} \right), \tag{11}$$

where

$$n = 0.75 - 1.27 \log F_c, \quad c = -0.4 - 0.67 \log F_c, \quad d = 0.14, \tag{12}$$

F_c is Troe parameter, and f_i are collisional efficiencies. Backward reaction rates are calculated from the principle of detailed balance using Gibbs potentials from [4]. Third body collisional efficiencies f_i for reactions No.5 through No.9 and No.15 were assumed equal to one unless noted otherwise in Table 2.

2.3 Equation of state

Thermodynamic properties of the reactants were taken from the Third Millenium thermochemical database [4]. For each reactant the database provides the molar specific heat at constant pressure, $C_{p,i}^o$ and the enthalpy, H_i^o, as a seven-term polynomial function of temperature T. Specific heat, enthalpy, internal energy, and pressure of the mixture are calculated as

$$\begin{aligned} &C_p(T, \mathcal{Y}_i) = \sum_{i=1}^{N} \mathcal{Y}_i C_{p,i}^o(T), \quad h(T, \mathcal{Y}_i) = \sum_{i=1}^{N} \mathcal{Y}_i H_i^o(T), \\ &e(T, \mathcal{Y}_i) = h - R_g T/\mathcal{M}, \quad \text{and} \quad P(\rho, T, \mathcal{Y}_i) = \rho R_g T/\mathcal{M}, \end{aligned} \tag{13}$$

Table 2: Reaction mechanism

	Reaction		A	β	E_a
1	$H + O_2 \rightleftharpoons O + OH$		1.91×10^{14}	0.00	16.44
2	$O + H_2 \rightleftharpoons H + OH$		5.08×10^{4}	2.67	6.292
3	$OH + H_2 \rightleftharpoons H + H_2O$		2.16×10^{8}	1.51	3.43
4	$O + H_2O \rightleftharpoons OH + OH$		2.97×10^{6}	2.02	13.4
$5^{(a)}$	$H_2 + M \rightleftharpoons H + H + M$		4.577×10^{19}	-1.4	104.4
$6^{(a)}$	$O_2 + M \rightleftharpoons O + O + M$		4.515×10^{17}	-0.64	118.9
$7^{(a)}$	$OH + M \rightleftharpoons O + H + M$		9.88×10^{17}	-0.74	102.1
$8^{(b)}$	$H_2O + M \rightleftharpoons H + OH + M$		1.912×10^{23}	-1.83	118.5
$9^{(c,*)}$	$H + O_2 + M \rightleftharpoons HO_2 + M$	k_o	3.48×10^{16}	-0.411	1.115
	$H + O_2 \rightleftharpoons HO_2$	k_∞	1.475×10^{12}	0.6	0
10	$HO_2 + H \rightleftharpoons H_2 + O_2$		1.66×10^{13}	0.00	0.823
11	$HO_2 + H \rightleftharpoons OH + OH$		7.079×10^{13}	0.00	0.295
12	$HO_2 + O \rightleftharpoons OH + O_2$		3.25×10^{13}	0.00	0.00
13	$HO_2 + OH \rightleftharpoons H_2O + O_2$		2.89×10^{13}	0.00	-0.497
$14^{(e)}$	$H_2O_2 + O_2 \rightleftharpoons HO_2 + HO_2$		4.634×10^{16}	-0.35	5.067
	$H_2O_2 + O_2 \rightleftharpoons HO_2 + HO_2$		1.434×10^{13}	-0.35	3.706
$15^{(d,*)}$	$H_2O_2 + M \rightleftharpoons OH + OH + M$	k_o	1.202×10^{17}	0	45.5
	$H_2O_2 \rightleftharpoons OH + OH$	k_∞	2.951×10^{14}	0	48.43
16	$H_2O_2 + H \rightleftharpoons H_2O + OH$		2.41×10^{13}	0.00	3.97
17	$H_2O_2 + H \rightleftharpoons H_2 + HO_2$		6.025×10^{13}	0.00	7.95
18	$H_2O_2 + O \rightleftharpoons OH + HO_2$		9.55×10^{6}	2.00	3.97
$19^{(e)}$	$H_2O_2 + OH \rightleftharpoons H_2O + HO_2$		1.0×10^{12}	0.00	0.00
	$H_2O_2 + OH \rightleftharpoons H_2O + HO_2$		5.8×10^{14}	0.00	9.557

(a) - $f_{H_2} = 2.5$, $f_{H_2O} = 12$.
(b) - $f_{H_2} = 0.73$, $f_{H_2O} = 12$.
(c) - $f_{H_2} = 1.3$, $f_{H_2O} = 14$.
(d) - $f_{H_2} = 2.5$, $f_{H_2O} = 12$.
(e) - sum of the two reactions.
(*) - Troe falloff, $F_c = 0.5$.

respectively, where where R_g is the gas constant and $\mathcal{M} = \left(\sum_{i=1}^{N} \mathcal{Y}_i\right)^{-1}$ is the mean molecular weight. The database also provides polynomials for Gibbs free energies G_i^0 used to calculate equilibrium constants and reverse reaction rates for the kinetic scheme Sect. 2.2.

2.4 Navier-Stokes terms

The viscous stress tensor, diffusion fluxes of individual reactants, and the diffusion energy flux associated with heat conduction and molecular diffusion in (2) - (4) are calculated as

$$\hat{\pi} = -\mu \left((\nabla \mathbf{u}) + (\nabla \mathbf{u})^T - (2/3)\hat{\mathbf{I}}(\nabla \cdot \mathbf{u}) \right), \tag{14}$$

where $\hat{\mathbf{I}}$ is the unit tensor and μ is the first physical viscosity coefficient,

$$\mathbf{q}^i = \rho \mathcal{Y}_i \mathbf{u}^i, \tag{15}$$

where $\mathbf{u}^i$ are diffusion velocities of reactants, and

$$\mathbf{q}^e = -\lambda \nabla T + \sum_{i=0}^{N} H_i^o \mathbf{q}^i, \tag{16}$$

where λ is the thermal conductivity coefficient.

The diffusion velocities $\mathbf{u}^i$ satisfy the well-known Stefan-Maxwell (SM) system of equations which relate $\mathbf{u}^i$ with spatial gradients of thermodynamical parameters and chemical composition [1]. The SM equations determine $\mathbf{u}^i$ up to an arbitrary constant; the value of the constant must be fixed by the requirement that the total mass diffusion flux of reactants is zero. Efficient methods of solving the SM equations for $\mathbf{u}^i$ have been thoroughly discussed in [5]. Following this paper, the SM equations and the zero mass flux condition can be written directly in terms of $\mathbf{q}^k$ as

$$\sum_{k=1}^{N} \Gamma_{ik} \mathbf{q}^k = \mathbf{g}_i, \tag{17}$$

and

$$\sum_{k=1}^{N} m_k \mathbf{q}^k = 0, \tag{18}$$

respectively, where

$$\Gamma_{ik} = (1 - \delta_{ik})\frac{\mathcal{Y}_i}{d_{ik}} - \delta_{ik}\sum_{j=1}^{N}\frac{(1 - \delta_{ij})\mathcal{Y}_j}{d_{ij}}, \tag{19}$$

$$\mathbf{g}_i = \mathcal{M}^{-1}\left(\nabla(\mathcal{M}\mathcal{Y}_i) - K_i^T\frac{\nabla T}{T} + (\mathcal{M} - m_i)\mathcal{Y}_i\frac{\nabla P}{P}\right). \tag{20}$$

Quantities d_{ij} in (19) are related to the ordinary binary diffusion coefficients D_{ij} as $d_{ij} = \frac{\rho}{\mathcal{M}}D_{ij}$; K_i^T are the thermal diffusion ratios, and δ_{ik} is the Dirac delta function. Both d_{ij} and K_i^T are density-independent, see Sect. 2.7. Vectors $\mathbf{g}_i$ are the combined gradients driving the diffusion of reactants. First term in (20) describes ordinary mass diffusion, the second term describes thermal diffusion (Soret effect), and the third term describes diffusion driven by a gradient of pressure. The heat diffusion caused by gradients of chemical composition (the Dufour effect) is small and has been ignored. The Soret effect is important for light reactants H and H_2. The pressure term may contribute in flows with strong vortices and rarefaction waves.

The solution of (17), (18) can be obtained as a convergent power-series expansion (see [5]),

$$\mathbf{q}^i = \sum_{k=0}^{\infty}\sum_{j=1}^{N} Q_{ij}^{[k]}\mathbf{q}_{HC}^j, \tag{21}$$

where

$$Q_{ij} = P_{ij} - d_j\sum_{m=1}^{N} P_{im}\Gamma_{mj}, \tag{22}$$

$$P_{ij} = \delta_{ij} - m_j\left(\sum_{k=1}^{N} m_k\right)^{-1}, \tag{23}$$

is the projection matrix which enforces the mass flux condition (18),

$$d_j = \frac{1 - m_j\mathcal{Y}_j}{\Gamma_{jj}}, \tag{24}$$

and

$$\mathbf{q}_{HC}^i = \sum_{j=1}^{N} P_{ij}d_j\mathbf{g}_j \tag{25}$$

is the projected Hirschfelder–Curtis approximation to diffusion fluxes; the superscript $[k]$ in (21) indicates a k-th power of Q. Exact solutions of (17), (18) can be obtained by solving the modified non-singular version of SM equations (see [5])

$$\sum_{k=1}^{N} \left(\Gamma_{ik} - \beta \left(m_i \mathcal{Y}_i \right) m_k \right) \mathbf{q}^k = \mathbf{g}_i, \tag{26}$$

where $\beta = const > 0$, using any standard algebraic method. In HSCD the diffusion fluxes are calculated using a truncated power-series solution (21) with three terms, $[k] = 0, 1, 2$; this provides the solution accuracy better than $\simeq 3\%$ as compared to the exact solution (26).

2.5 Viscosity coefficient

Physical viscosity of a mixture is calculated according to [6, 7] as

$$\mu = \sum_{i=1}^{N} \frac{\mu_i \mathcal{Y}_i}{G_i^{\mu}}, \tag{27}$$

where

$$G_i^{\mu} = \sum_{k=1}^{N} \left(\delta_{ik} + \frac{1 - \delta_{ik}}{2\sqrt{2}} \phi_{ik} \right) \mathcal{Y}_k, \tag{28}$$

$$\phi_{ik} = \left(1 + \frac{\sigma_i}{\sigma_k} \right)^2 \left(1 + \frac{m_i}{m_k} \right)^{1/2}, \tag{29}$$

and

$$\mu_i = \frac{2.669 \times 10^{-5} \sqrt{m_i T}}{\sigma_i^2 \Omega^{(2,2)}(T_i^*)}, \tag{30}$$

are viscosities of individual reactants [1], $T_i^* = T/\epsilon_i$ is the reduced temperatures, σ_i and ϵ_i are the Lennard-Jones cross-sections and potential parameters, respectively, and $\Omega^{(2,2)}$ is the dimensionless Lennard-Jones collisional integral given as a function of reduced temperature T^* in Appendix M-I of [1]. Table 3 lists values of σ_s and ϵ_s used in HSCD; they are adopted from the GRI-Mech database [8].

Table 3: Lennard-Jones parameters

Reactant	ϵ, ^{o}K	σ, Å
H	145.0	2.05
H_2	38.0	2.92
O	80.0	2.75
O_2	107.4	3.458
OH	80.0	2.75
H_2O	572.0	2.605
HO_2	107.4	3.485
H_2O_2	107.4	3.4558

2.6 Thermal conductivity coefficient

Thermal conductivity of a mixture was calculated according to [1, 9, 7],

$$\lambda = \sum_{i=1}^{N} \frac{\lambda_i \mathcal{Y}_i}{G_i^c}, \tag{31}$$

where

$$G_i^c = \sum_{k=1}^{N} \left(\delta_{ik} + \frac{1.065}{2\sqrt{2}} \left(1 - \delta_{ik}\right) \phi_{ik} \right) \mathcal{Y}_k \tag{32}$$

and ϕ_{ik} are given by Equation (29). Coefficients of thermal conductivity for individual species corrected for the transfer of energy between translational and internal degrees of freedom are calculated according to [1],

$$\lambda_i = E_i \lambda_i^0, \tag{33}$$

where

$$\lambda_i^0 = \frac{8.322 \times 10^3}{\sigma_s^2 \Omega^{(2,2)}(T_i^*)} \sqrt{\frac{T}{m_i}} = 3.12 \times 10^8 \frac{\mu_i}{m_i} \tag{34}$$

are uncorrected coefficients of thermal conductivity and

$$E_i = 1 + 0.354 \left(\frac{C_{p,i}^0}{R_g} - \frac{5}{2} \right), \tag{35}$$

are the correction (Eucken) factors.

2.7 Mass diffusion coefficients

Binary diffusion coefficients and thermal diffusion ratios are calculated according to [1, 7] as

$$D_{ik} = \frac{\mathcal{M}}{\rho} d_{ik}, \tag{36}$$

and

$$K_i^T = \frac{\mathcal{M}}{R_g} \sum_{k=1}^{N} \frac{1.2\, C_{ik}^* - 1}{d_{ik}} \left(\frac{\mathcal{Y}_i m_i a_k - \mathcal{Y}_k m_k a_i}{m_i + m_k} \right), \tag{37}$$

respectively, where

$$d_{ik} = \frac{2.265 \times 10^{-5}}{\sigma_{ik}^2} \left(\frac{m_i + m_k}{m_i m_k} \right)^{1/2} \frac{\sqrt{T}}{\Omega^{(1,1)}(T_{ik}^*)}, \tag{38}$$

$$\begin{aligned} \sigma_{ik} &= \frac{\sigma_i + \sigma_k}{2}, \quad a_i = \frac{\lambda_i^0}{G_i^c}, \\ C_{ik}^* &= \frac{\Omega^{(1,2)}(T_{ik}^*)}{\Omega^{(1,1)}(T_{ik})}, \quad T_{ik}^* = \frac{T}{\sqrt{\epsilon_i \epsilon_k}}, \end{aligned} \tag{39}$$

and $\Omega^{(1,1)}$, $\Omega^{(1,2)}$ and dimensionless collisional integrals are also provided as a function of reduced temperature T^* in Appendix I-M of [1].

3 Numerical method

The numerical method was selected based on several requirements. First, the method must be able to treat both the continuous flow and the shock waves with a sufficient accuracy. Second, it must incorparate a stable and robust stiff integration method for chemical terms. Third, it must provide a temporal and spatial numerical resolution to properly treat reaction fronts, boundary layers, sound waves, and turbulence. Forth, numerical calculations must be feasiblly performed on existing supercomputers in a reasonable time. The target machine for the project was a ten petaflop BG/Q Mira at Argonne which has 786, 432 processors, which means that the numerical method must have good scaling properties. The HSCD code has been created with the above requirements in mind. The code was developed using the BG/P Intrepid and BG/Q Mira computers at Argonne, computer resources were provided by the DoE INCITE program during the years 2010-2014, and the Early Science Program (ESP) at Argonne during the year 2013.

3.1 Hydrodynamics

The code is based on the distributed memory parallel adaptive mesh refinement (AMR) reactive flow solver [10, 11] which is augmented with the multicomponent equation of state (EOS), microscopic transport (Navier-Stokes terms), and chemical kinetics suitable for hydrogen combustion, described above. The current version of HSCD runs in a hybrid OpenMP/MPI mode and scales up to the entire BG/Q Mira. In practice, due to the queuing policies the production simulations were performed utilizing either one third or two thirds of the entire machine.

To integrate the Euler part of the hydrodynamical equations (1) - (4) the HSCD uses a directionally split Godunov-type second-order accurate conservative algorithm. Numerical fluxes are evaluated using a monotone linear reconstruction and a Riemann solver [12, 13]. Viscous, thermal, and mass diffusion fluxes are calculated using second-order central differencing and added to Eulerian fluxes. Reactions are treated using a stiff ODE solver and coupled to a hydrodynamical integration via a process split with sub-sycling.

3.2 Adaptive mesh refinement

A distinct feature of the code is a highly dynamic cell-by-cell AMR based on a parallel fully threaded tree (FTT) structure. In ordinary trees pointers are directed from parents to children. In FTT, the pointers are inverted and directed from groups of children to parents and parent's siblings. This arrangement eliminates expensive tree searches which are notoriously difficult to parallelize and it allows all operations, including mesh refinement and derefinement, to be performed in parallel. The mesh is refined around shocks, discontinuities and in regions containing large gradients of physical variables such as chemical variables, temperature, vorticity, and so on. AMR is performed every fourth time step after which the cells are rebalanced across the processors using a heuristic to estimate the amount of work required by the cells, maintain data locality, and minimize communications across MPI ranks. The FTT library automatically synchronizes the data in ghost cells after global operations. The code can run in the uniform grid and static mesh refinement modes as well.

3.3 Integration of stiff reaction terms

During a chemical step the HSCD integrates a stiff sub-system of (1) – (4),

$$\frac{d\mathbf{Y}}{dt} = \mathbf{R}, \tag{40}$$

where

$$\mathbf{Y} = \begin{bmatrix} \mathcal{Y}_1 \\ \mathcal{Y}_2 \\ ... \\ \mathcal{Y}_N \\ T \end{bmatrix}, \quad \mathbf{R} = \begin{bmatrix} \mathcal{R}_1 \\ \mathcal{R}_2 \\ ... \\ \mathcal{R}_N \\ -\left(\frac{\partial e}{\partial T}\right)^{-1} \sum_{k=1}^{N} \left(\frac{\partial e}{\partial \mathcal{Y}_k}\right) \mathcal{R}_k \end{bmatrix}, \tag{41}$$

assuming $\rho = const$. For a stiff ODE solver to be practical as a part of a fluid dynamics code the solver must utilize information at only one time layer, be able to deal with extremely stiff equations, and be inexpensive. HSCD uses a non-iterative, single step solver [14],

$$\left(\hat{I} - \Delta t \hat{J}^o\right) (\mathbf{Y}^n - \mathbf{Y}^o) = \delta t \mathbf{F}^o \ , \tag{42}$$

where

$$\hat{J}(t) = \frac{\partial \mathbf{F}}{\partial \mathbf{Y}} \tag{43}$$

is a Jacobian of $\mathbf{F}$, and superscripts o and n indicate variables at the beginning and the end of a chemical step of integration, δt. The solver is first-order accurate and is unconditionally stable. YASS turns into an explicit first-order Euler method when $\delta t \to 0$. YASS reduces to

$$\mathbf{Y}^n = \mathbf{Y}^o - \left(\hat{J}^o\right)^{-1} \mathbf{F}^o \ , \tag{44}$$

when $\delta t \to \infty$; this is a Newton-Raphson iteration step for the solution of the equilibrium equation $\mathbf{F}(\mathbf{Y}_{eq}) = 0$. A solution will converge quadratically to a true equilibrium if it is already brought into the radius of convergence in the process of integration. By construction, YASS conserves the sum of mass fractions of chemical species with machine accuracy when $\hat{J}$ is calculated precisely. The HSCD calculate derivatives of $\mathbf{F}$ with respect to $\mathbf{Y}$ analytically. Accuracy of integration of individual components of $\mathbf{Y}$ depends of course on Δt which must satisfy usual requirements $|Y_i^n - Y_i^o|/Y_i^o < \epsilon < 1$ for $Y_i > f > 0$. Recommended values are $\epsilon = 10^{-3}$ and $f = 10^{-8}$. Sub-cycling is used when the chemical step δt becomes shorter than the hydrodynamical time step determined from the Courant stability criteria.

3.4 Hybrid OpenMP/MPI programming model

The application algorithms in HSCD are programmed in terms of work functions executed by global iterators. This allowed a clean hierarchical hybridization of the code and implementation of an OpenMP/MPI programming model. In the MPI code FTT iterators are executed on all MPI ranks. On each rank, an iterators parses the local mesh into constant-length chunks and feeds them to a work-function. The iterator returns when all chunks are processed. Conversion to OpenMP/MPI was accomplished by splitting the chunks of cells into smaller sub-chunks and applying workfunctions to sub-chunks on each MPI rank in parallel using OpenMP. This approach affects the outermost loops of the application code and leads to a very coarse-grained OpenMP parallelism. For example, flux calculation and updates of computational cells in the code are programmed within a single loop inside one of the work-functions. The OpenMP parallelization of the loop consisted of creating a single parallel region and guarding the small section of the code responsible for final updates of physical quantities inside the loop. Strong scalability of the code is shown on Figure 1.

4 Code verification and validation

We are assembling a suite of validation data for the physical models required in first-principles DDT simulation. The components include: the equation of state; transport processes including multi-species diffusion, viscosity, and heat transfer; and the chemical kinetics mechanism. In addition, a hierarchy of model problems representing components of the DDT process have been identified. These are designed to cover ignition and laminar flames, flame acceleration and boundary layer development, hot-spot formation, and propagating detonation. Recent efforts have concentrated on modeling reflected shock tube ignition delay experiments and studies of a reflected shock-boundary layer interaction, Section 4.1.

The implementations of the EoS and transport coefficients were verified by comparison the Cantera calculations; which is an open source chemical kinetics and thermodynamics package written by Dr. David Goodwin, Caltech. Using a high temperature extrapolation, thermodynamic data are valid for temperatures up to 6000 K. Comparison of transport coefficients as a function of temperature were carried out for each of the single gas species, as well

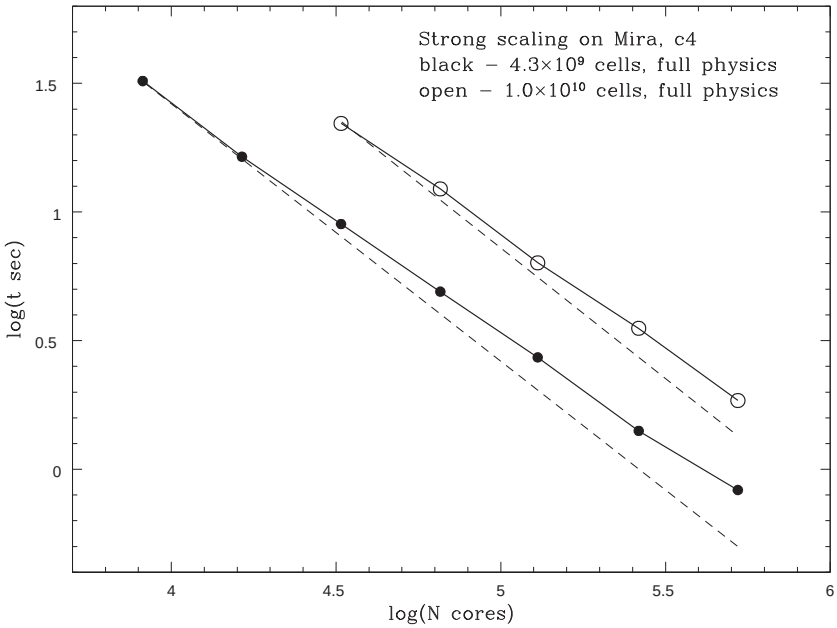

Figure 1: Typical scaling characteristics of HSCD on BG/Q Mira. Shown is strong scaling on two problems of different size, 4.3×10^9 computational cells and 10^{10} computational cells, with full physics, dynamic AMR performed everey fourth time step, and full checkpointing performed every 100 time steps. Scaling data were collected from two hundres consequtive time steps during production runs performed on up to 524288 cores (two thirds of the machine) in OpenMP/MPI mode with 16 OpenMP threads per MPI rank.

as a multi-species mixture created from a linearly independent combination of mole fractions.

The chemical kinetics mechanism selected for HSCD is that of O Conaire et al [2]. The mechanism has its origin in Yetter [15], which was later modified by Kim [16]; the current version builds on the mechanism of Mueller [17]. This mechanism has been validated in the past by a large number of researchers across several different types of flows including shock tube ignition delay experiments (temperatures and pressures: 965-1200 K, 1 atm; 1250-1800 K, 3 atm; 1650-1930 K, 3-64 atm; 1100-1520 K, 1 atm); flame speed measurement (pressures 1-20 atm, equivalence ratios 0.5 - 3.5); high pressure flame speed measurements (pressures 1-20 atm, equivalence ratios 0.5 - 3.5); lean H_2/air and H_2/air/CO_2 flame speed measurements (temperatures 750-900K, 1 atm, equivalence ratios 0.3-0.7); burner stabilized flames (pressure 0.05 atm, equivalence ratio 1.91); comprehensive flow reactors (temperatures 880-935 K, pressures 0.3-15.7 atm).

4.1 Numerical simulations of a shock bifurcation

The first documented experimental observation of the shock bifurcation phenomena was by Mark [18]. Strehlow and Cohen [19] observed boundary layer interaction with the reflected shock for all gases except helium and argon. More recently, Petersen and Hanson [20] investigated the extent and magnitude of the bifurcation region for variety of different conditions. The above experiments were all conducted in shock tubes with circular cross-section. The experiments of Brossard et al. [21] were carried out in a facility with a test section of 72 $\times$ 72 mm initial cross-section. Schlieren images in [21] show a complex three-dimensional structure during shock reflection. Overall, the onset of a bifurcated (Mach) reflection in a square channel is similar to that in axisymmetric geometries. However, the experiments show intriguing differences caused by square geometry, in particular, the deformation and retardation of the boundary layer separation line is observed near the channel corners.

The selection of the shock bifurcation as a validation test has the following motivation: (1) the ignition delay experiments are used for measuring reaction rates and experimental validation of chemical kinetic mechanisms. Once a chemical mechanism is incorporated into a three-dimensional DNS numerical model, the ability of numerically reproducing measured ignition delays provides a validation test. (2) reflection of an incident shock produces

strong three-dimensional effects including shock bifurcation, formation of recirculation bubbles and turbulent jets. The magnitude of the effects depends on input physics, tube geometry, and wall boundary conditions including wall roughness and heat conduction through the walls. (3) details of shock reflection also dependent on the development and growth of a boundary layer behind the incident shock. All these processes may have a varying degree of influence on the ignition in the reactive gas during ignition delay measurements, and these same processes are among the constituent hydrodynamical processes affecting the DDT. The DNS simulations of reflected shock tube experiments provide a rich opportunity for validating a large complex of physical effects important for first-principles modeling of the DDT.

As a first step of the validation program we initiated three-dimensional viscous Navier-Stokes simulations of shock reflection in CO_2 in conditions of the experiments of Brossard et al. [21]. Figure 2 shows the computational setup. After the shock reflects off the end wall, the reflected shock bifurcates and forms a complex structure consisting of the main reflected shock in the center of the tube and the oblique shock near the walls of the tube, Figure 3. Comparison of the simulation with the experiment is shown in Figure 4. An excellent agreement has been obtained with the position of the shock, the heigth of the bifurcated structure, and the angles formed by the primary and secondary reflected shocks.

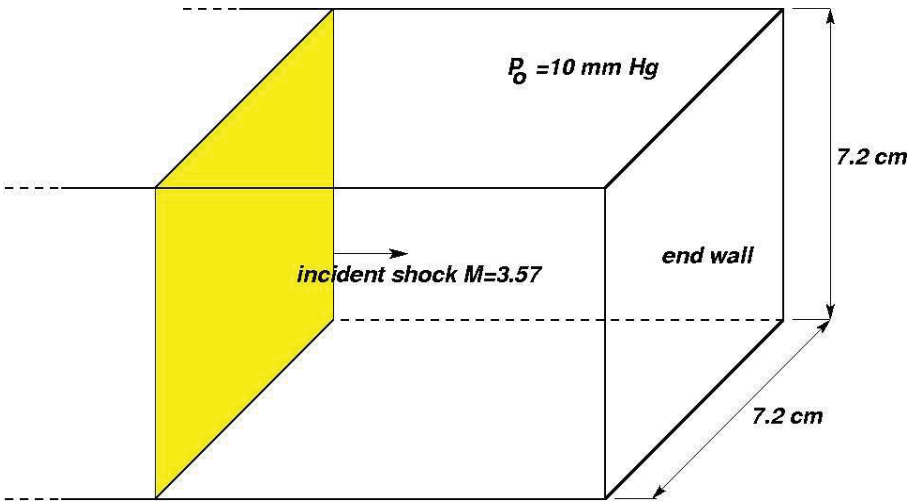

Figure 2: Bifurcation of a reflected shock in CO_2 in a square shock tube. Computational setup corresponds to the experiment [21]. The incident shock wave with Mach number $M = 3.57$ propagates towards the end wall of the tube (to the right).

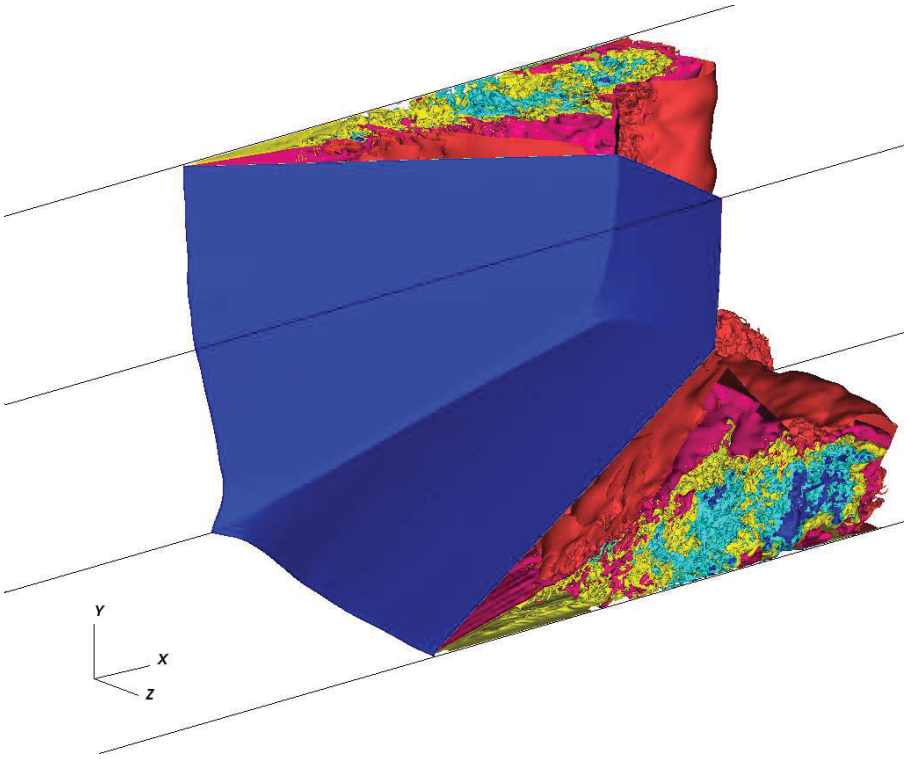

Figure 3: Shock wave reflection in CO_2 - contours of constant density shown in one quarter of the computational domain. Blue is the surface of the bifurcated reflected shock.

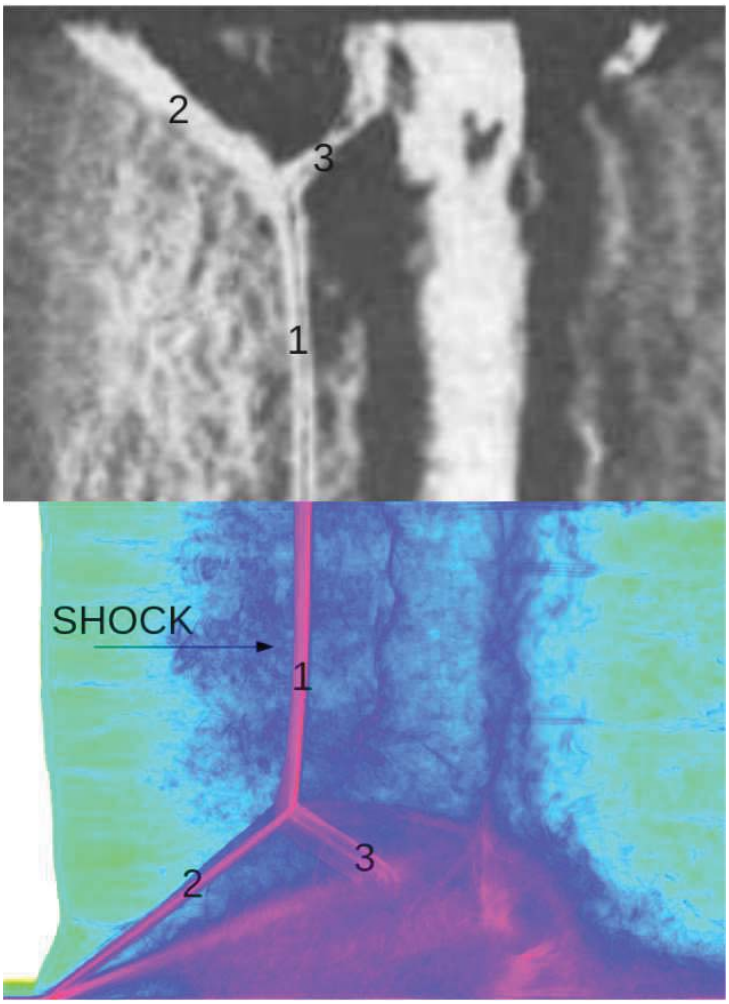

Figure 4: Schlieren images of the bifurcated reflected shock in CO_2 in a square shock tube. Top - experiment [21]. Bottom - numerical simulation. (1) - primary reflected shock. (2) - oblique shock. (3) - secondary shock. Shocks are moving to the left.

4.2 Strong and mild ignition in hydrogen-oxygen

Strong and mild ignition regimes were first observed in reflected shock tube experiments in $2H_2+O_2$ in [23, 22]. For sufficiently strong shocks the ignition occurs at the end wall of the tube and leads to an immediate onset of a detonation wave (strong ignition). With decreasing M the ignition moves away from the wall and takes place in hot spots which form multiple flame kernels. The flame kernels merge and give rise to a detonation at a later time (mild ignition). The main goal of the validation simulations described in this section was to reproduce both ignition regimes and compare the numerically found boundary between the regimes with the experiments.

The simulations of strong and mild ignition were carried out in conditions of experiments [26]. The authors documented their experimental setup in sufficient details so that the calculations matching the experimental geometry and initial conditions were possible. The computational setup of the simulations is shown in Figure 5. Fig. 6 illustrates the main features of the

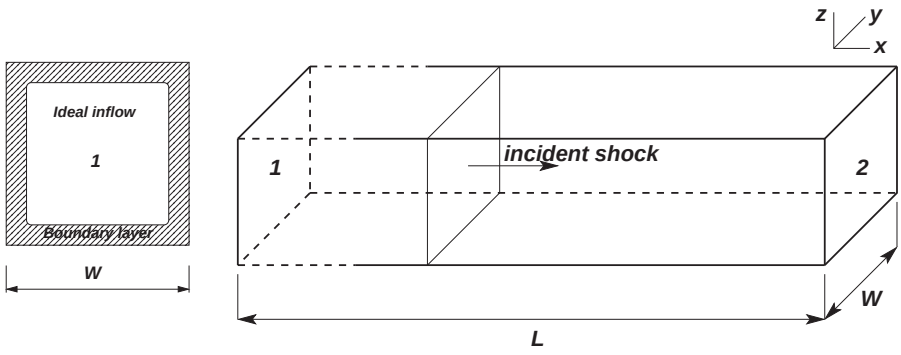

Figure 5: Right - computational domain, 1 - inflow, 2 - end wall. Left - inflow boundary conditions: white area - ideal post-shock inflow, dashed area - post-shock boundary layer.

reflection. After the incident shock reaches the end wall, the reflected shock, (R1), begins to propagate back to the inflow boundary. Interaction of (R1) with the boundary layer created by the incident shock leads to shock bifurcation and the formation of the λ-structure made of the inclined forward shock (R2) and a secondary shock (R3). In the middle of the tube the matter passes from the region (1) through the (R1) shock into the region (2) where it remains nearly stationary. Close to the walls the incoming matter passes

through the shocks (R2) and (R3) and continues to flows towards the end wall under the slip line (SL). Part of the flow is redirected in the stagnation region (SR) into the recirculation jet (J) and begins to move to the left, toward (R2). Remaining matter passes through (SR) and continues to slowly flow through the region (3) toward the end wall. A pseudo-schlieren image of the shock region illustrates a true three-dimensional structure of the reflected shock region with highly distorted (R1) and (R2) shocks, and with multiple secondary shocks. The recirculation region behind the reflected shock, (J) and (SR), is violently unstable, contains sonic turbulence, and continuously sheds vortices. The vortex shedding is accompanied by the generation of acoustic and entropy perturbations. The latter serve as initial sites of developing hot spots which later trigger the ignition of matter. Depending on the Mach number of the incident shock the ignition leads to either the detonation wave or to multiple flame kernels and mild ignition. Figure 7 shows images of the hot spot ignition which took place $\simeq 0.5$ cm from the end wall and near the corner formed by the two side walls of the tube. The ignition of the hot spots gave rise to flame kernels shown in Fig. 7a,b. The visible flame velocity estimated from the simulation was $\simeq 300$ m/s, which translates to a flame velocity $S \simeq 30 - 40$ m/s relative to matter. The flame propagated in the nearly $P \simeq const$ regime with average $P \simeq 25$ atm and $\simeq 20\%$ pressure variations across the kernels. The slightly elevated pressure ahead of the growing flame quickly changed the temperature in the surrounding gas and triggered a a detonation visible in Fig. 7c. The expansion velocity of the detonation kernel is $\simeq 1.5$ km/s and the pressure inside the kernel is $P \simeq 180$ atm, significantly larger than that in the surrounding material. Figure 8 shows the case of strong ignition when the shock strength is increased. The transition between strong and mild ignition regimes at $M \simeq 1.72 - 1.75$ is consisten with the experiment.

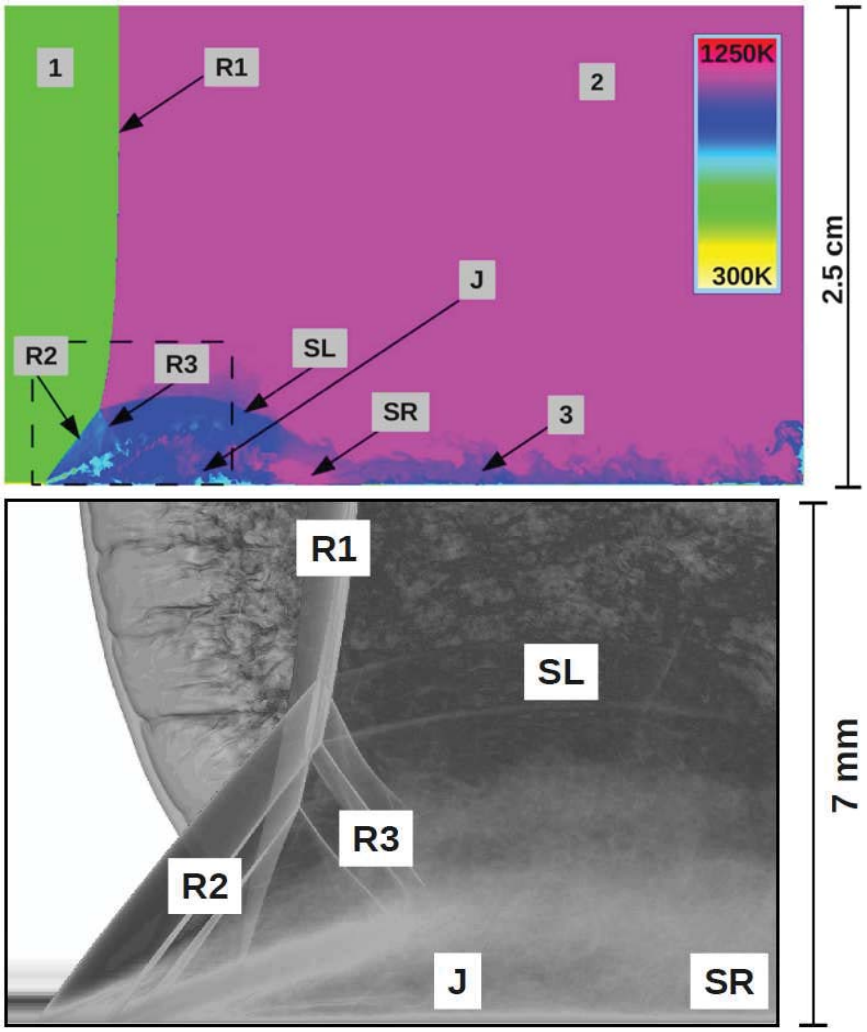

Figure 6: Shock wave reflection in $2H_2 + O_2$. Top - two-dimensional temperature distribution in the center-plane of the tube at $t = 62.80$ μs after reflection. Reflected shock is moving to the left. Bottom - pseudo-schlieren image of the reflected shock area (dashed line).

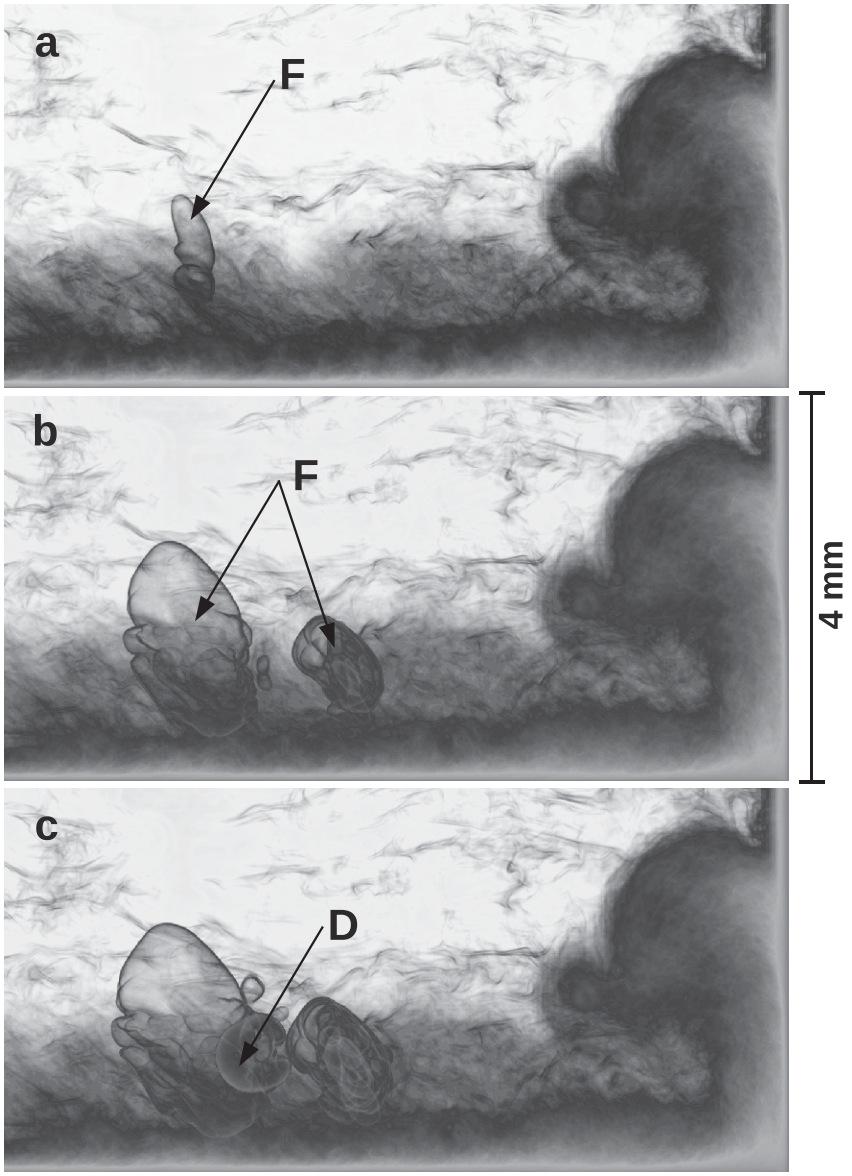

Figure 7: Mild ignition in $2H_2 + O_2$ at Mach number $M = 1.72$. Numerical pseudo-schlieren images of the lower right corner of the shock tube. F - flame kernels. D - detonation kernel. Times are (a) - 61.38 μs , (b) - 62.62 μs, and (c) - 62.96 μs after shock reflection.

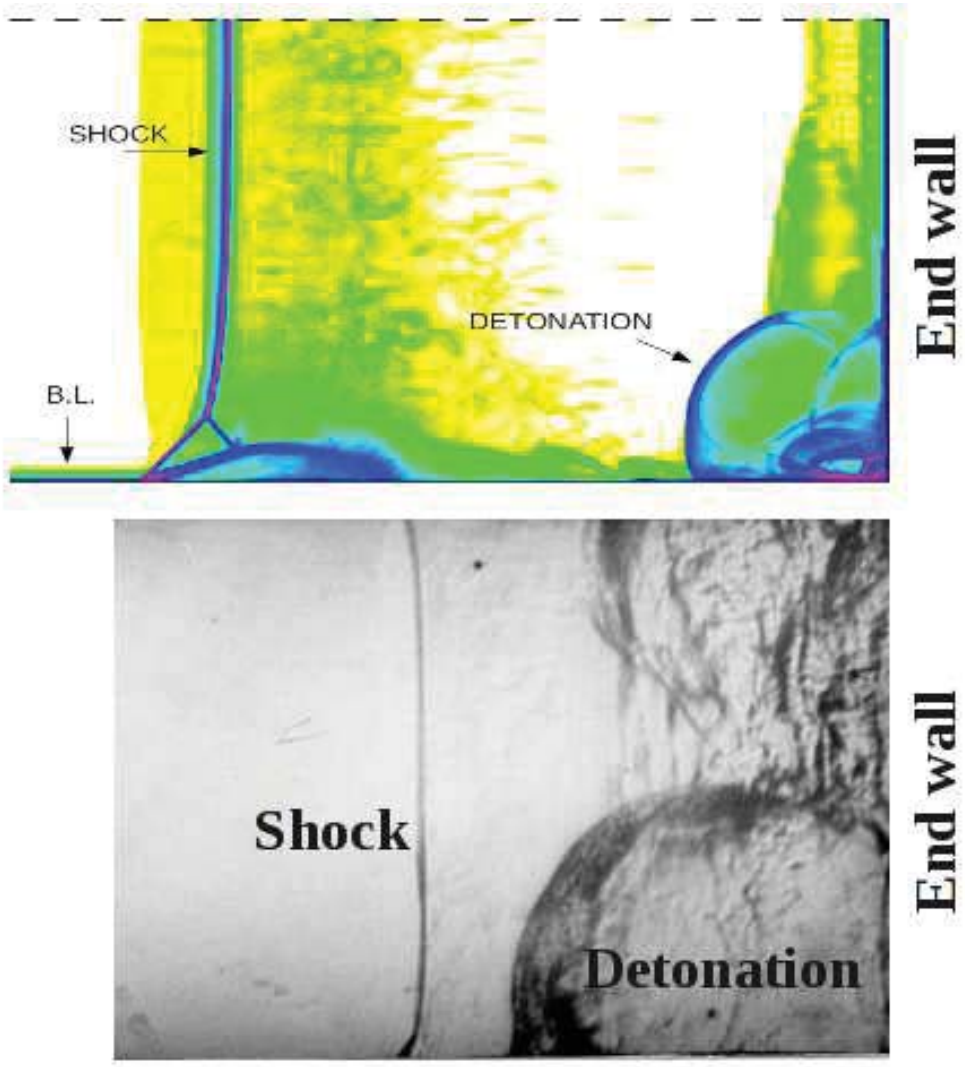

Figure 8: Strong ignition in $2H_2 + O_2$. Top - numerical pseudo-schlieren images of the lower right corner of the shock tube when Mach number is $M = 1.75$. Ignition does not lead to multiple flame kernels. The detonation is formed directly via the explosion of an isolated hot spot in the lower right corner of the tube. Bottom - a representative experimental schlieren image of a strong ignition process in a reactive gas [27].

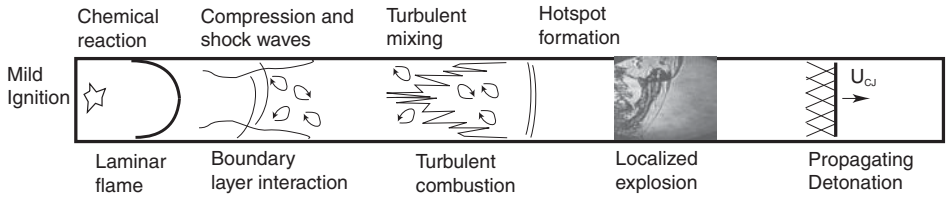

Figure 9: Schematic of a DDT experiment.

5 Flame acceleration and DDT in a long pipe

Schematic of a typical shock tube DDT experiment is shown in Figure 9. The flame is ignited near the end wall of the tube (at the left). The flame kernel grows and the flame surface becomes distorted and the flame eventually becomes turbulent. As the flame accelerates along the tube it generates a series of shocks moving ahead of the flame. Eventually the acceleration leads to a localized explosion and the onset of a detonation wave.

The simulation of the flame acceleration process was performed for conditions of the experiments reported in [28, 29, 30]. The rectangular tube had a cross-section of 1×1.25 square in. The ambient pressure $P = 1$ atm and ambient temperature $T = 300$K. The walls were modeled with the no-slip isothermal boundary conditions. The spark was located flush at the end wall of the tube and the spark energy 0.01 Jouls was released at a constant rate during 3 μsec. The ignition process generated an outgoing shock wave and a laminar flame kernel. The Ignition process and the early stage of the flame development is illustrated in Figure 10. In this figure the weak pressure disturbance generated by the spark and the shape of the flame surface is compared with the experimental schlieren image from [28]. One of the difficulties with the simulation of the spark ignition on the computer is that the experimental rate of the energy release and the exact shape of the spark region are unknown. The agreement between the simulated and experimental position of the outgoing shock is reasonably good. The experimental shape of the flame shows some asymmetry.

Figure 11 shows a sequence of numerical schlieren images of the flame acceleration process. The accelerating flame is unstable and it generates a sequence of the pressure and shock waves which eventually coalesce into a strong leading shock moving along the shock tube ahead of the flame brush. The detonation was observed to originate in highly compressed and heated matter in the region close ahead of the flame brush. The simulation reproduced one of the modes of the DDT observed in the experiments, Figure 12, although the experimental picture is significantly more complicated and asymmetric, and may have been affected by wall irregularities (see [30]).

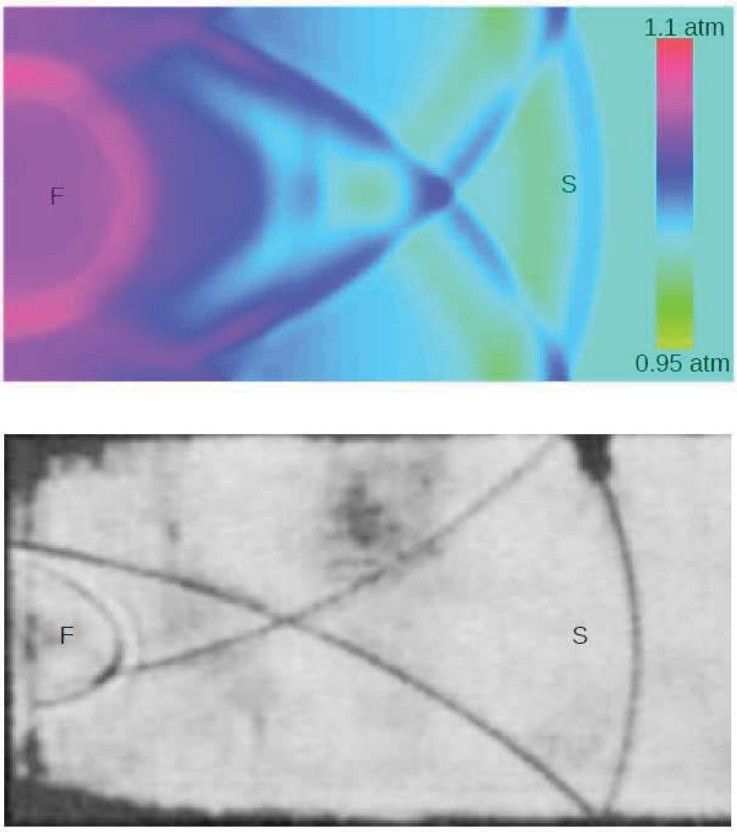

Figure 10: Spark ignition process. Top - simulation. Bottom - experiment [28].

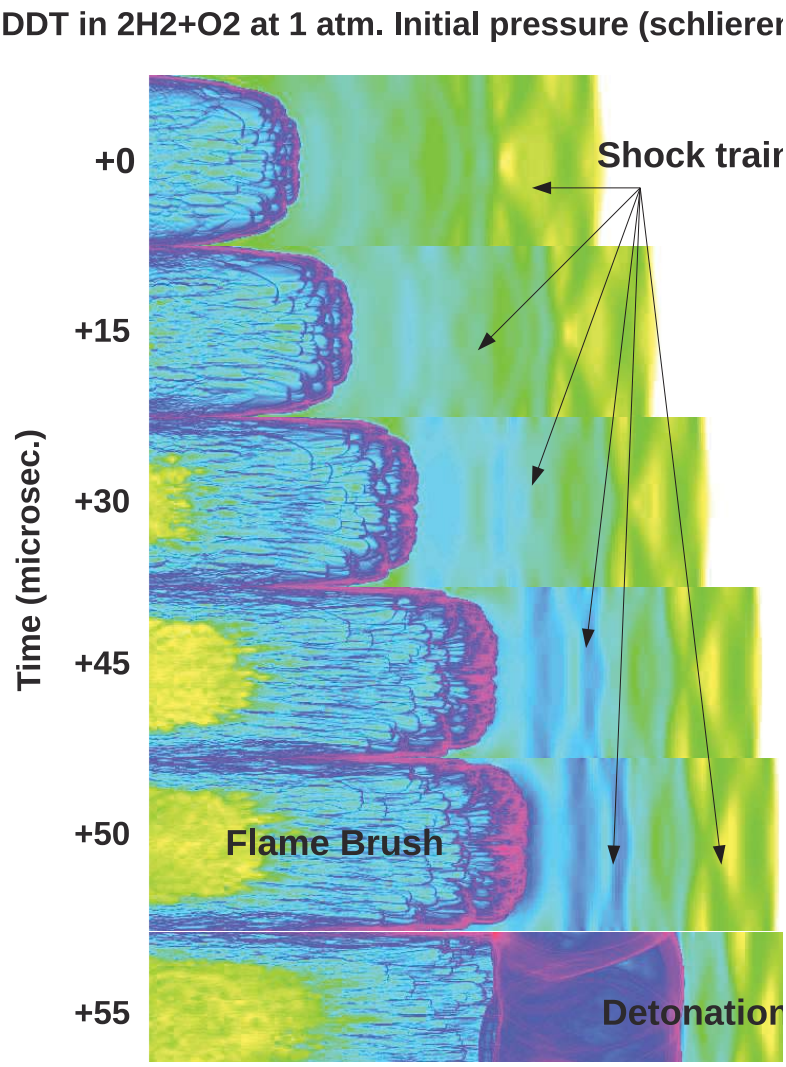

Figure 11: Flame acceleration and DDT in a $2H_2 + O_2$ mixture in 1×1.25 square inch tube. The figure shows numerically generated pseudo-schlieren images. The detonation emerged at some moment of time between the last two frames. The DDT took place in a hot compressed matter situated between the accelerating flame and the leading shock.

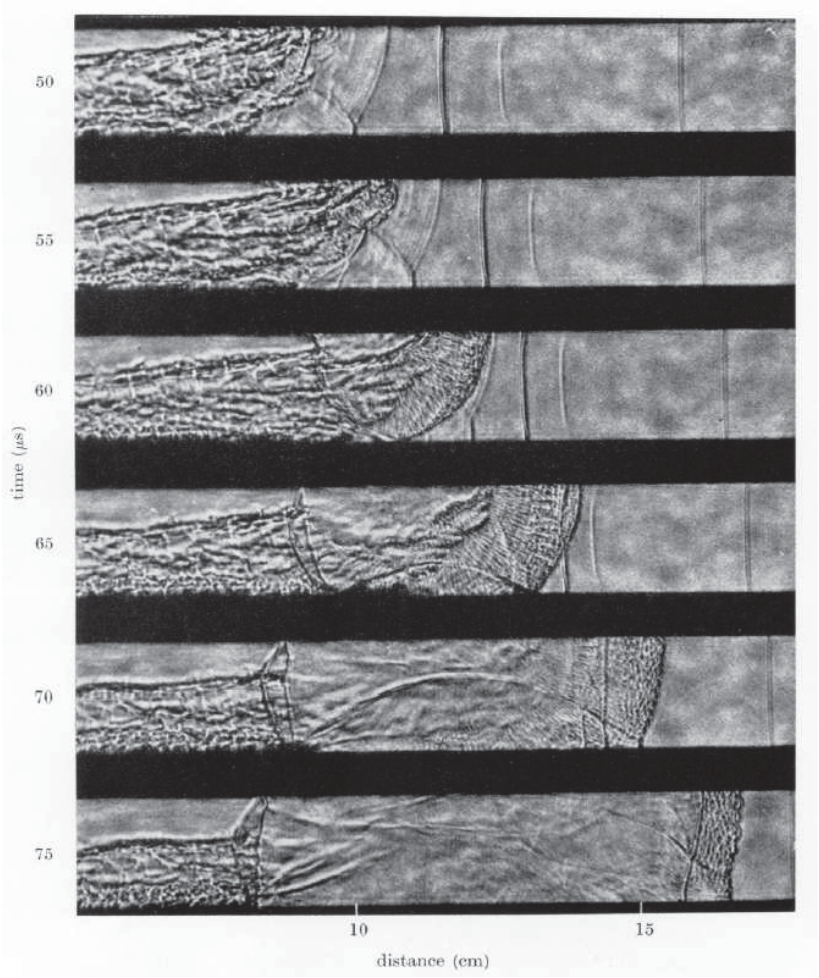

Figure 12: Schlieren images of the onset of a detonation in one of experiments [30].

6 Conclusions

The main products of this project are

(1) a working high speed combustion and detonation numerical code, HSCD, capable of simulating compressible combustion and detonation phenomena in hydrogen-oxygen mixtures. The HSCD code is a distributed memory parallel code which is optimized for running on the largest supercomputers such as BG/Q Mira at Argonne National Laboratory. The code also runs on parallel Linux clusters, workstations, and laptops on which a Linux operation system is installed. The source code of HSCD is provided as a part of the report.

(2) The demonstration DNS simulation of the flame acceleration and DDT in a $2H2 + O_2$ mixture.

References

[1] J.O. Hirschfelder and C.F. Curtiss and R.B. Bird (1954). Molecular Theory of Gases and Liquids, John Wiley & Sons, Inc., New York.

[2] M.O. Conaire and H.J. Curran and J.M. Simmie and W.J. Pitz and C.K. Westbrook (2004). A Comprehensive Modeling Study of Hydrogen Oxidation. Int. J. Chem. Kinet. 36:603–622.

[3] R. G. Gilbert, K. Luther and J. Troe (1983). Ber. Bunsen-Ges. Phys. Chem., 87: 169

[4] A. Burkat and B. Ruscic (2005). Third Millennium Ideal Gas and Condensed Phase Thermochemical Database for Combustion with Updates from Active Thermochemical Tables, ANL-05/20, Chicago, IL, USA.

[5] V. Giovangigli (1991). Convergent iterative Methods for Multicomponent Diffusion. Impact of Computing in Science and Engineering, 3:244–276.

[6] C.R. Wilke (1950) A Viscosity Equation for Gas Mixtures. The Journal of Chemical Physics, 18:517-519.

[7] E.S. Oran and J.P.Boris (1987). Numerical Simulation of Reactive Flow, Elsevier Science Publishing, Inc., New York.

[8] http://www.me.berkeley.edu/gri_mech/

[9] E.A. Mason and S.C. Saxena (1958). Approximate Formulas for the Thermal Conductivity of Gas Mixtures. Physics of Fluids, 5:139–146.

[10] A. Khokhlov (1988), Fully Threaded Tree Algorithms for Adaptive Refinement Fluid Dynamics Simulations. J. Comput. Phys., 143:519–543.

[11] A.M. Khokhlov, A.Yu. Chtchelkanova, *Fully Threaded Tree Algorithms for Massively Parallel Computations*, in Proceedings of the Ninth SIAM Conference on Parallel Processing for Scientific Computing, San Antonio, Texas, USA, March 22-24, 1999.

[12] B. van Leer (1979), Towards the Ultimate Conservative Difference Scheme. V. A second-Order Sequel to Godunov's Method, JCP, 32:101–136.

[13] P. Colella and H.M.Glaz, (1985). Efficient Solution Algorithms for the Riemann Problem for Real Gases, JCP, 59:264-289.

[14] A. Khokhlov, I. Dominguez, C. Bacon, etal. (2012), Three-dimensional Simulations of Thermonuclear Detonation with α-Network: Numerical Method and Preliminary Results, Advances in computational astrophysics: methods, tools, and outcome. Proceedings of a conference held at Cefalu, Italy 13 - 17 June 2011. ASP Conference Proceedings, Vol. 453. Edited by R. Capuzzo-Dolcetta, M. Limongi, and A. Tornambe. San Francisco: Astronomical Society of the Pacific, 2012., p.107.

[15] R.A. Yetter, F.L. Dryer, and H. Rabbitz. *Combust. Sci. Tech.*, 79:97–128, 1991.

[16] T.J. Kim, R.A. Yetter, and F.L. Dryer. In *Proc. Combust. Inst.*, volume 25, pages 759–766, 1994.

[17] M.A. Mueller, R.A. Yetter, and F.L. Dryer. *Int. J. Chem. Kinet*, 31:113–125, 1999.

[18] H. Mark. The interaction of a reflected shock wave with the boundary layer in a shock tube. *NACA Technical Memo*, 15:333–340, 2006.

[19] R. Strehlow and A. Cohen. Limitations of the reflected shock technique for studying fast chemical reactions and its application to the observation of relaxation in nitrogen and oxygen. *Journal of Chemical Physics*, 30:257–265, 1959.

[20] E L. Petersen and R K. Hanson. Measurement of a reflected-shock bifurcation over a wide range of gas composition and pressure. *Shock Waves*, 15:333–340, 2006.

[21] J. Brossard, N. Charpentier, T. V. Bazhenova, V.P. Fokeev, A. A. Kalachev, and A.I. Kharitonov. Experimental study of shock wave reflection in a narrow channel. In *Proceedings of the 15th International Symposium on Shock waves and Shock Tubes*, pages 163–169, 1984.

[22] Voevodsky, V. V. and Soloukhin, R. I. (1965). On the mechanism and explosion limits of hydrogen-oxygen chain self-ignition in shock waves. Symposium (International) on Combustion, 10:279-283.

[23] R.A. Strehlow and A. Cohen (1962). Initiation of Detonation. Phys. Fluids, 5:97-101.

[24] J.W. Meyer and A.K. Oppenheim (1971). On the shock-induced ignition of explosive gases. Thirteenth Symposium (International) on Combustion, 13:1153-1164.

[25] J.W. Meyer and A.K. Oppenheim (1971). Coherence theory of the strong ignition limit. Combust. Flame, 17:65-68.

[26] M. Steinberg and W.E. Kaskan (1955), Initiation of Detonation, Phys. Fluids, 5:97-101.

[27] G.O. Thomas and R. Bambrey (2002), Some observations of the controlled generation and onset of detonation, Shock Waves, 12:13-21.

[28] A.J. Laderman and P.A. Urtiew and A.K. Oppenheim, (1962). Effect of ignition geometry on initial flame acceleration in a spark ignited explosive gas, Combustion and Flame, 6:325–335.

[29] A.J. Laderman and P.A. Urtiew and A.K. Oppenheim, (1963). Dynamics of the generation of pressure waves by accelerating flames, Symposium (International) on Combustion, 9:265–274.

[30] P.A. Urtiev and A.K. Oppenheim, (1966). Experimental observations of the transition to detonation in an explosive gas, Proceedings of the Royal Society of London. Series A, Mathematical and Physical Sciences, 295:13–40.